Ceramics International 47 (2021) 18351–18357

Contents lists available at ScienceDirect

Ceramics International

journal homepage: www.elsevier.com/locate/ceramint

Fabrication of in-situ self-reinforced Si_3N_4 ceramic foams for high-temperature thermal insulation by protein foaming method

Feiyue Yang [*,1], Yiwen Yao [1], Zichun Yang, Shuang Zhao, Guobing Chen, Kunfeng Li

School of Power Engineering, Naval University of Engineering, 717 Jiefang Avenue, Wuhan, 430032, China

ARTICLE INFO

Keywords:
Self-reinforced ceramic foams
Microstructure
Thermal conductivity
Compressive strength
High-temperature oxidation resistance

ABSTRACT

To meet demand for lightweight and high-strength ceramic foams, in-situ self-reinforced Si_3N_4 ceramic foams, with compressive strength of 13.2–45.9 MPa, were fabricated by protein foaming method combined with sintered reaction-bonded method. For comparison, ordinary protein foamed ceramics with irregular block microstructure were fabricated via reaction-bonded method, which had compressive strength of 3.6–20.5 MPa. Physical properties of these two types of samples were systematically compared. When open porosity was about 80%, both types of Si_3N_4 ceramic foams had excellent thermal insulation properties (<0.15 W m^{-1} K^{-1}), while compressive strength of in-situ self-reinforced samples increased by more than 158% compared with ordinary samples. Under high-temperature oxidation conditions, microstructures of both types of samples were deformed with increase in oxidation temperature. Moreover, after oxidation temperature was increased to 1400 °C, oxidation weight gain decreased from 18.07% for ordinary samples to only 2.18% for self-reinforced samples. Thus, high-temperature oxidation resistance of Si_3N_4 ceramic foams was greatly improved.

1. Introduction

Silicon nitride (Si_3N_4) ceramic foams have excellent wear resistance, high-temperature resistance, and corrosion resistance of Si_3N_4, as well as the properties of light weight, high specific surface area and excellent air permeability of porous ceramics [1–5]. These excellent features of Si_3N_4 ceramic foams make them widely used in high-temperature filters, catalyst carriers, thermal insulation materials, etc. [6–9]. Generally, the cost of preparing porous ceramics using Si_3N_4 powder as a raw material is relatively high [10,11]. Therefore, the fabrication of Si_3N_4 ceramics by reaction-bonded method with the advantages of cheap and easy processing has great potential for engineering applications.

Stable three-dimensional structure plays an important role in improving the mechanical properties of ceramic foams, while high porosity leads to their low mechanical strength. In order to enhance the mechanical properties of ceramic foams, researchers have adopted methods such as doping other particles (Y_2O_3 [12], metals [13], La_2O_3 [14], CeO_2 [15]) and self-growing whiskers [16]. For instance, Das et al. [9] fabricated mullite porous ceramics with a bending strength of 38.4 MPa by doping SiC particles (with open porosity of 36.4%), which increased the strength of the material by about 30%. Moreover, optimizing the preparation process is also an effective method to improve the mechanical properties of porous ceramics. For example, by optimizing the viscosity of slurry and idle time of gelation during gel injection molding, Parsi et al. [2] successfully fabricated Si_3N_4 porous ceramics with bending strength of 182 MPa. Currently, the research in this field is focused on exploring more environment-friendly and convenient methods to prepare Si_3N_4 porous ceramics with excellent mechanical properties.

When materials such as Si_3N_4 and SiC are used in high-temperature fields, it is necessary to prevent hot-gas corrosion and high-temperature oxidation from weakening their performance. For extending the service life of materials at high temperatures, various methods have been widely investigated, including doping substances [17], surface pretreatment [18,19], and spray coating [20]. Lenz et al. [21] prepared anti-oxidation coatings on Si_3N_4 substrates, and found that the coating containing X_2-Yb_2SiO_5 and $Yb_2Si_2O_7$ exhibited the lowest corrosion rate (−1.8 μg cm^{-2}·h^{-1}) under high-temperature (1400 °C) and humid environments. For materials with multiple different crystal forms such as Si_3N_4 (α-Si_3N_4, β-Si_3N_4, γ-Si_3N_4) and ZrO_2 (m-ZrO_2, t-ZrO_2, c-ZrO_2), their high-temperature characteristics are related to the crystal form of the material, which is attracting the attention of many researchers.

* Corresponding author.
E-mail address: feiyuemit@163.com (F. Yang).
[1] Co-first authors: F. Yang and Y. Yao contributed equally to this work.

https://doi.org/10.1016/j.ceramint.2021.03.156
Received 7 January 2021; Received in revised form 15 February 2021; Accepted 17 March 2021
Available online 20 March 2021

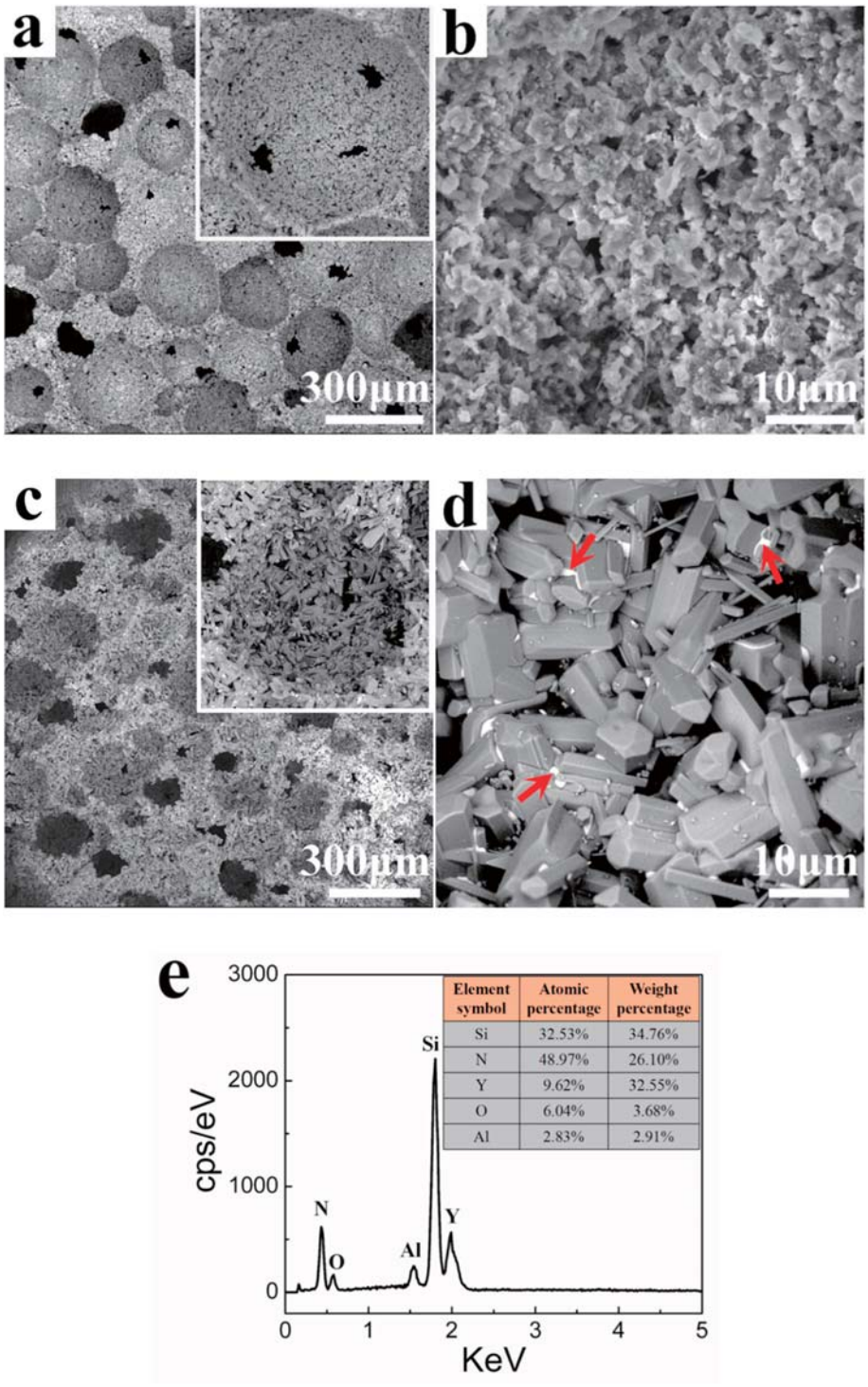

Fig. 1. (a) Pore distribution and (b) pore wall microstructure of the sample fabricated by reaction-bonded method; (c) pore distribution, (d) pore wall microstructure and (e) EDS spectrum of intergranular phase of the sample fabricated by sintered reaction-bonded method.

In order to fabricate ceramic foams with high-strength and high-temperature resistance, in-situ self-reinforced Si_3N_4 ceramic foams were fabricated by protein foaming method combined with sintered reaction-bonded method in this work. For comparison, ordinary protein foamed ceramics were fabricated by reaction-bonded method. Then, the differences in the microstructure and properties (including open porosity, density, compressive strength, thermal conductivity and high-temperature oxidation resistance) of both types of samples were systematically investigated.

2. Materials and methods

Commercial silicon (Si) powder (D_{50} = 3 μm, purity > 99.9%, ForsmanScientific, China) was used as raw material. In addition, 3 wt% Al_2O_3 and 5 wt% Y_2O_3 powder (based on the weight of Si powder) were added as sintering aids. The above raw materials were mixed and stirred for 4–6 h in a ball mill (at speed of 250 rpm). Then, deionized water was added to the slurry and it was stirred for 2 h. After that, 12 wt% protein powder (based on the weight of Si powder) was added to the mixed

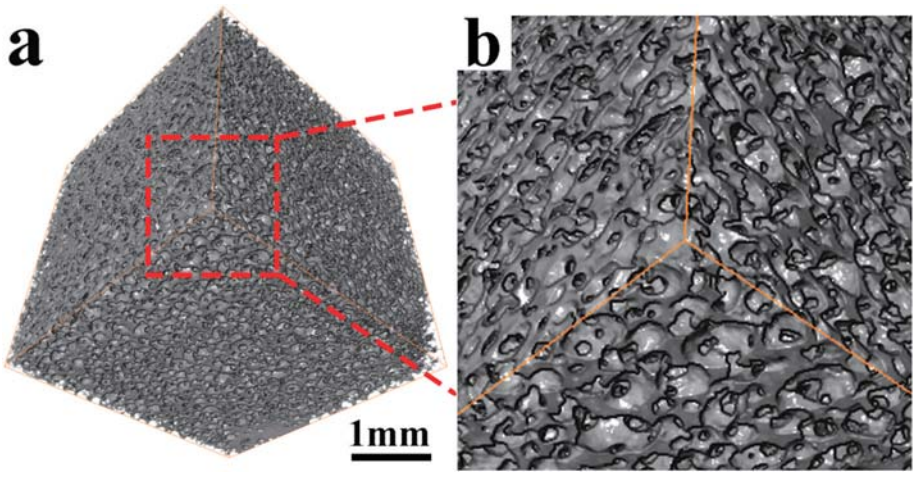

Fig. 2. Three-dimensional CT images of the sample fabricated by sintered reaction-bonded method.

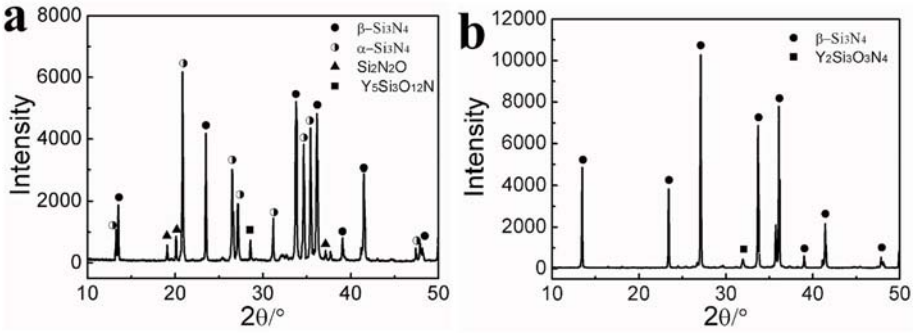

Fig. 3. XRD patterns of samples fabricated by different sintering methods: (a) reaction-bonded method; (b) sintered reaction-bonded method.

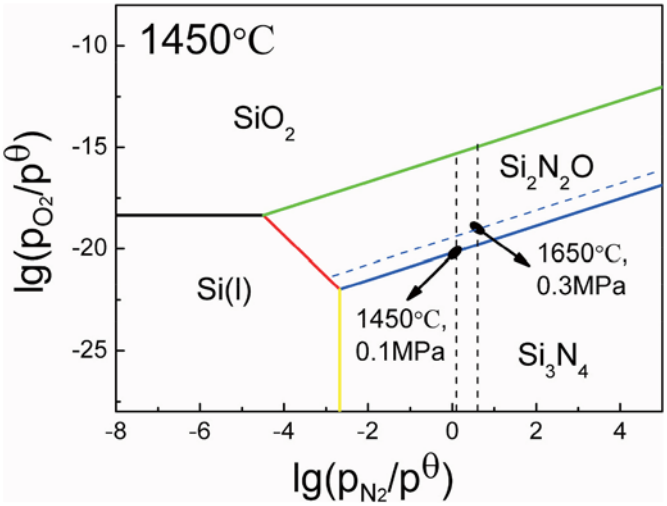

Fig. 4. Phase stability diagram of Si–O–N system at 1450 °C.

slurry and stirred for 1 h (at speed of 350 rpm). Then the foamed slurry was injected into a mold and cured in a drying oven at 80 °C for 2 h. After demolding, green bodies were dried and then placed in a high-temperature furnace for debinding at 600 °C for 2 h. Finally, green bodies were sintered by the following two methods: (1) The samples were reaction-bonded at 1450 °C for 6 h under 0.1 MPa nitrogen (purity = 99.99%, $O_2 \leq 20$ ppm) pressure; (2) the samples were first reaction-bonded at 1450 °C for 6 h (0.1 MPa N_2), and then post-sintered at 1650 °C for 3 h under a nitrogen pressure of 0.3 MPa.

Microstructure of the sample was characterized by scanning electron microscopy (SEM, Phenom XL, USA) equipped with an energy dispersive spectrometer (EDS). An X-ray computed tomography (CT) scanner (nanoVoxel 2000, China) with a resolution of 500 nm was used to detect the three-dimensional (3D) structure of the sample (10 × 10 × 10 mm). The phase composition of the sample was analyzed via X-ray diffraction (XRD, Bruker D8, Germany) with a scanning range of 10°–50°, and the scanning speed was 5°/min. The density and open porosity of the sample were evaluated using the method based on Archimedes' principle. The sample was drilled into a cylinder with dimension of φ20 × 20 mm for compressive strength tests using a mechanical tester (MTS CMT6103, USA) with a crosshead speed of 0.5 mm/min. Four specimens were used to determine the average compressive strength of the sample. The thermogravimetric analysis of the sample was performed by a synchronous thermal analyzer in the temperature range from room temperature to 1400 °C (10 °C/min). The thermal conductivity of the sample at room temperature was tested via thermal conductivity meter (Hot Disk TPS 2500S, Sweden). A high-temperature furnace was used to oxidize the samples at different temperatures for 2 h, and the heating rate was 5 °C/min.

3. Results and discussion

3.1. Microstructure and phase composition

The pore distribution and pore wall microstructure of protein foamed ceramics fabricated by reaction-bonded method and sintered reaction-bonded method are shown in Fig. 1a–d. The pore morphology of both types of samples presented typical spherical structures, as shown in the

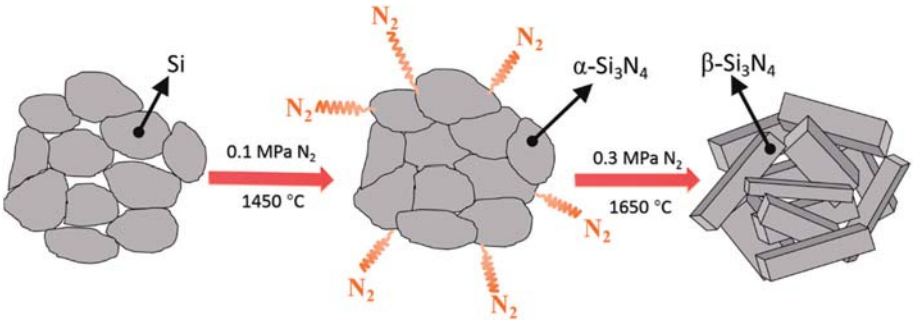

Fig. 5. Schematic diagram of the synthesis of in-situ self-reinforced ceramic foams.

Table 1
Physical properties of samples fabricated by different sintering methods.

Samples fabricated by different methods	Open porosity (%)	Density ($g \cdot cm^{-3}$)	Thermal conductivity ($W \cdot m^{-1} \cdot K^{-1}$)	Compressive strength (MPa)
Reaction-bonded method	83.81	0.44	0.114	3.6 ± 0.3
	78.94	0.53	0.136	5.1 ± 0.9
	66.46	0.86	0.302	8.0 ± 1.2
	45.08	1.47	0.771	20.5 ± 2.3
Sintered reaction-bonded method	79.97	0.57	0.147	13.2 ± 1.7
	75.32	0.71	0.188	14.9 ± 1.5
	62.03	1.08	0.665	28.2 ± 3.1
	49.29	1.48	1.412	45.9 ± 5.4

low-magnification SEM images (Fig. 1a and c). Moreover, the microstructure of the pore walls of samples fabricated by reaction-bonded method appeared as irregular blocks (Fig. 1b). However, the microstructure of the sample fabricated by sintered reaction-bonded method presented overlapping and interlocking crystal columns (Fig. 1d), with obvious ridge lines (marked by red rectangle in Fig. 1d). In addition, there were some obvious small white particles between crystal columns (shown by red arrow in Fig. 1d), which were found to be the Si–N–O–Al–Y intergranular phase after analyzing the EDS pattern (Fig. 1e). Previous studies have found that the sintering aids in the sample, such as Al_2O_3 and Y_2O_3, can react with each other to form the intergranular phase at high temperatures [14]. Furthermore, the three-dimensional CT images of the sample fabricated by sintered

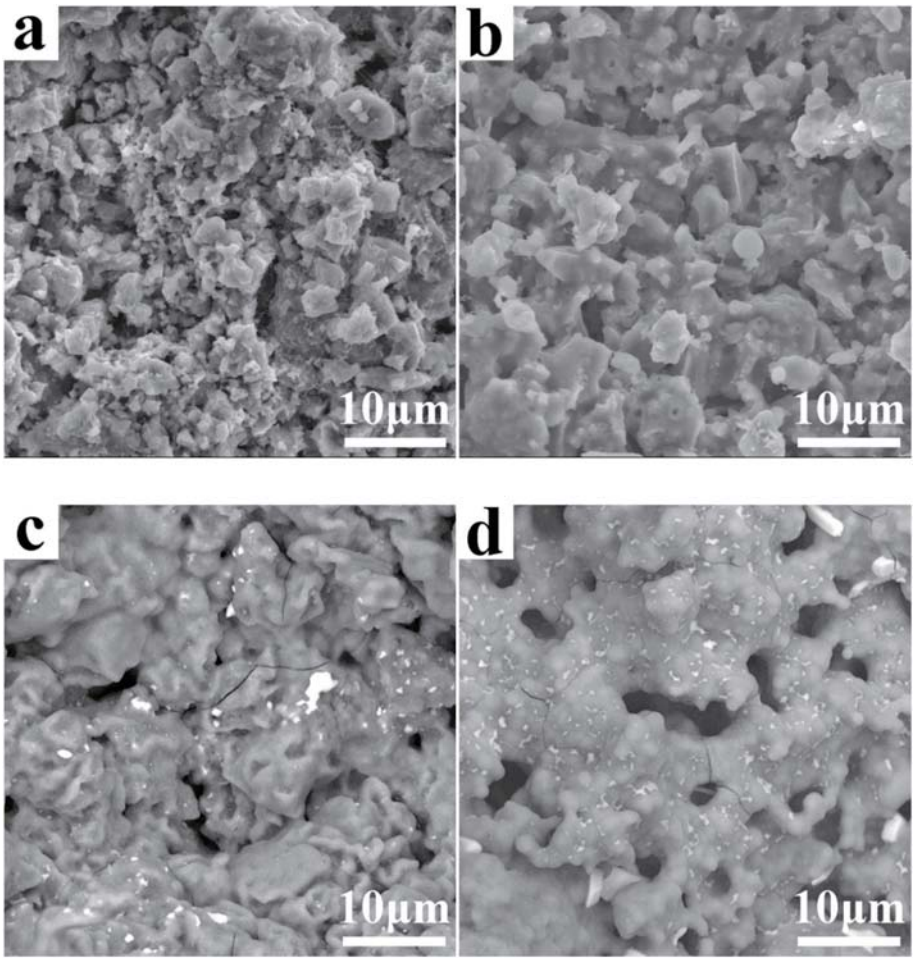

Fig. 6. Microstructures of samples fabricated by reaction-bonded method after oxidation at different temperatures: (a) 800 °C; (b) 1000 °C; (c) 1200 °C; (d) 1400 °C.

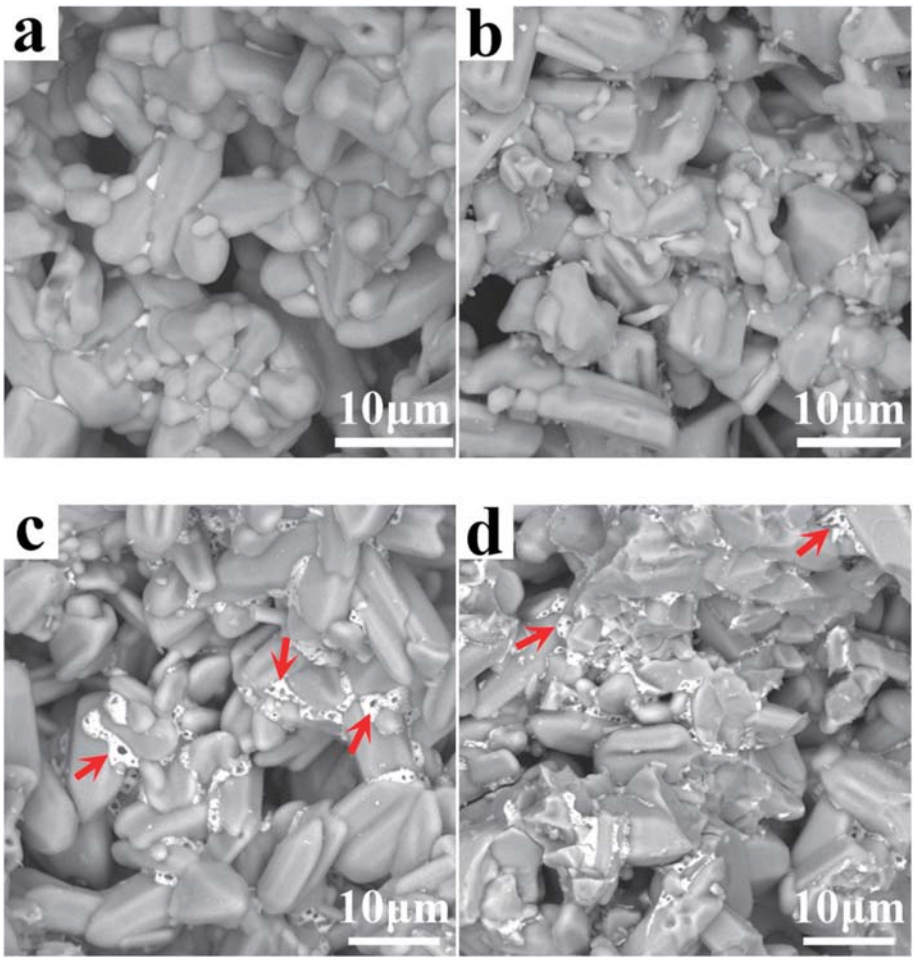

Fig. 7. Microstructures of samples fabricated by sintered reaction-bonded method after oxidation at different temperatures: (a) 800 °C; (b) 1000 °C; (c) 1200 °C; (d) 1400 °C.

reaction-bonded method are presented in Fig. 2a and b. As can be seen, the sample presented an obvious foam structure with uniform pore size distribution, indicating the effectiveness of the protein foaming method for fabricating ceramic foams.

The phase composition of both types of sintered samples was analyzed by XRD pattern, as shown in Fig. 3. The results show that the main phase of both types of samples was α-Si_3N_4 and β-Si_3N_4 respectively, but they both contained a small amount of Si–N–O–Al–Y intergranular phase. Moreover, small amounts of β-Si_3N_4 and Si_2N_2O phases were present in the samples fabricated by reaction-bonded method.

The above reaction system can be regarded as an Si–N–O system, and the effects of trace O_2 in nitrogen ($O_2 \leq 20$ ppm) and pressure of nitrogen on the reaction process can be further analyzed by thermodynamic calculation [22–24]. For the samples fabricated by reaction-bonded method, the phase stability diagram (Fig. 4) of Si–O–N system at 1450 °C (1723 K) was plotted after thermodynamic calculation. It can be seen that Si first reacted with nitrogen and trace O_2 to form Si_2N_2O (Equation (1)) during sintering process. Hence, a small amount of Si_2N_2O appeared in the XRD pattern (Fig. 3a) of the samples fabricated by reaction-bonded method. Meanwhile, the thin SiO_2 layer on the surface of the Si particles might also undergo a reduction reaction to form Si_2N_2O (Equation (2)), resulting in a further increase in the content of Si_2N_2O. As the oxygen partial pressure decreased below the critical value (shown by point A in Fig. 4), Si and N in the Si–O–N system underwent a nitridation reaction, continuously forming irregular block α-Si_3N_4 (Equation (3)). Furthermore, the sintering aids (Al_2O_3 and Y_2O_3) promoted the liquid phase sintering of Si_3N_4, resulting in a phase transition of α→β in part of α-Si_3N_4. Therefore, both α-Si_3N_4 and β-Si_3N_4 phases existed in the sample.

$$2Si(l) + N_2(g) + 0.5O_2(g) \rightarrow Si_2N_2O(s) \quad (1)$$

$$1.5Si(l) + 0.5SiO_2(s) + N_2(g) \rightarrow Si_2N_2O(s) \quad (2)$$

$$3Si(l) + 2N_2(g) \rightarrow \alpha - Si_3N_4(s) \quad (3)$$

$$3Si_2N_2O(s) + N_2(g) \rightarrow 2\alpha - Si_3N_4(s) + 1.5O_2(g) \quad (4)$$

$$\alpha - Si_3N_4(s) \rightarrow \beta - Si_3N_4(s) \quad (5)$$

The schematic diagram in Fig. 5 illustrates the synthesis process of in-situ self-reinforced Si_3N_4 ceramic foams fabricated by sintered reaction-bonded method. After reaction sintering at 1450 °C, the sample continued to be sintered at 1650 °C under 0.3 MPa nitrogen pressure. At this time, the critical oxygen partial pressure required for the forming of Si_3N_4 in the Si–N–O system was increased, as shown by point B in Fig. 4. This prompted Si_2N_2O to proceed in the direction of the forming of Si_3N_4 (Equation (4)). In addition, the increase in nitrogen pressure can accelerate the nitridation reaction, inhibit the evaporation of intermediate reaction gases such as SiO, and promote the nucleation and growth of Si_3N_4 [25]. Moreover, under high-temperature conditions, the α→β phase transition of α-Si_3N_4 promoted the formation of β-Si_3N_4 crystal columns (Equation (5)), which conforms to the dissolution-precipitation mechanism [26,27]. The above reaction mechanism promoted the

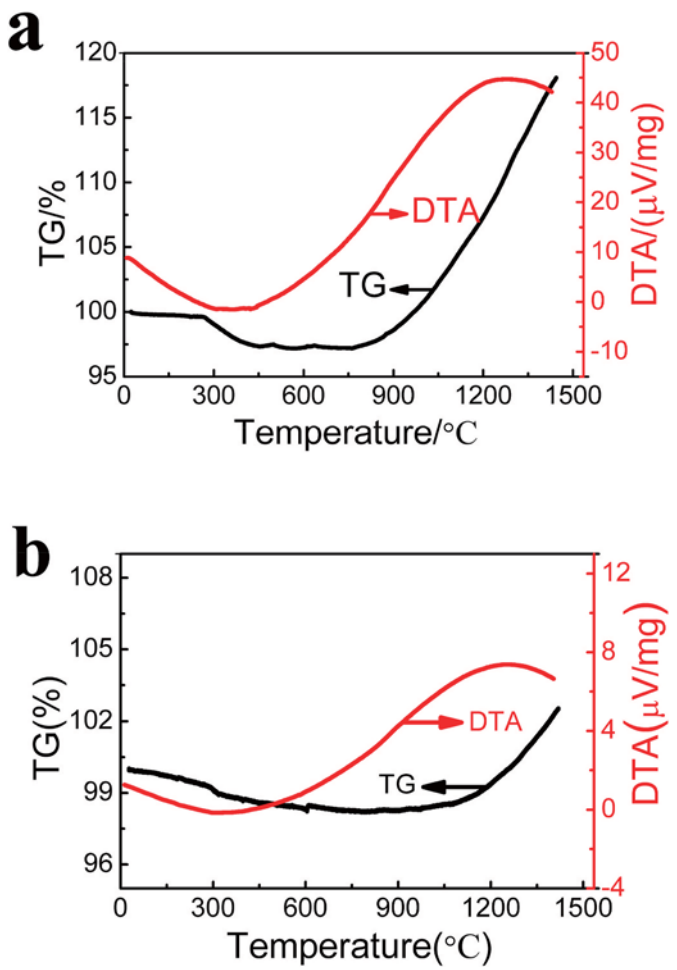

Fig. 8. TG-DTA curves of samples fabricated by different sintering methods: (a) reaction-bonded method; (b) sintered reaction-bonded method.

reduction of α-Si_3N_4 and Si_2N_2O phases in the in-situ self-reinforced samples. Also, the Si–N–O–Al–Y intergranular phases were precipitated and distributed between β-Si_3N_4 crystal columns.

3.2. Open porosity, thermal conductivity and compressive strength

Table 1 summarizes the physical properties such as open porosity, density, thermal conductivity and compressive strength of Si_3N_4 ceramic foams fabricated by two different sintering methods. With the decrease in open porosity, it can be found that the thermal conductivity and compressive strength of both types of sintered samples tended to increase. Besides, when the open porosity was approximately the same, thermal conductivity of the in-situ self-reinforced samples fabricated by sintered reaction-bonded method was significantly higher than that of the ordinary samples fabricated by reaction-bonded method. This was mainly due to the higher thermal conductivity of the β-Si_3N_4 crystal column than that of irregular bulk α-Si_3N_4. It is worth noting that both types of samples with high porosity (open porosity > 75%) had low thermal conductivity (<0.15 W m^{-1} K^{-1}), which met the requirements of thermal insulation materials.

Furthermore, when the open porosity was approximately the same, the compressive strength of in-situ self-reinforced sample was significantly higher than that of ordinary sample fabricated by reaction-bonded method. Especially for samples with high open porosity of about 80%, the compressive strength of in-situ self-reinforced samples (13.2 MPa, open porosity = 79.97%) increased by more than 158% compared with ordinary samples (5.1 MPa, open porosity = 78.94%). This phenomenon could be explained by the following two aspects: (1) The microstructure of in-situ self-reinforced sample presented overlapping and interlocking β-Si_3N_4 crystal columns, forming a stable three-dimensional structure. Such a structure enhanced the mechanical properties of the material [4]. (2) There was an obvious Si–N–O–Al–Y intergranular phase between β-Si_3N_4 crystal columns of the in-situ self-reinforced sample (Fig. 1d), which promoted the tighter integration of crystal columns. Owing to above two enhancement mechanisms, the compressive strength of in-situ self-reinforced samples was significantly improved. In comparison, the microstructure of ordinary sample fabricated by reaction-bonded method presented irregular blocks with poor mechanical stability of the three-dimensional structure, resulting in low compressive strength.

3.3. High-temperature oxidation resistance

The high-temperature oxidation resistance of Si_3N_4 ceramic foams has an important influence on their application in high-temperature fields. The microstructures of ordinary samples fabricated by reaction-bonded method after oxidation at different temperatures are shown in Fig. 6a–d. It can be seen that after oxidation at 800–1000 °C, the microstructure of the samples still appeared as irregular blocks. When the oxidation temperature was increased to 1200 °C, the irregular block structure began to show fusion bonding, which became more intense as the temperature increased. However, for the in-situ self-reinforced samples fabricated by sintered reaction-bonded method, the ridge lines of the crystal columns (marked by red rectangle in Fig. 1d) disappeared at high temperature, which resulted in the β-Si_3N_4 crystal columns becoming "smooth" at high temperatures. Nevertheless, the microstructure of the sample still basically consisted of overlapping and interlocking crystal columns (Fig. 7a–d). Also, after oxidation at the temperature range of 1200–1400 °C, obvious small pores appeared on the surface of the Si–N–O–Al–Y intergranular phase between crystal columns (Fig. 7c and d). These pores were likely formed by the reaction between the intergranular phase and oxygen at high temperatures, which generated a small amount of gas.

The high-temperature oxidation resistance of the samples was further investigated by thermogravimetric analysis. The TG curves of both types of sintered samples showed obvious weight loss at about 300 °C (Fig. 8), which may be due to the decomposition of some impurities with low melting points. Moreover, for the ordinary samples fabricated by reaction-bonded method and the in-situ self-reinforced samples fabricated by sintered reaction-bonded method, the TG curves indicated that their initial temperatures of accelerated oxidation were about 900 °C and 1050 °C, respectively. Also, after the oxidation temperature was increased to 1400 °C, oxidation weight gain of both samples was 18.07% and 2.18%, respectively. The above results indicated that the high-temperature oxidation resistance of the in-situ self-reinforced Si_3N_4 ceramic foams was significantly better than that of ordinary samples. This phenomenon may be attributed to the superior chemical stability of crystalline columnar β-Si_3N_4 compared to irregular block α-Si_3N_4, making it more difficult to react with O_2 [11,20].

4. Conclusion

In this work, in-situ self-reinforced ceramic foams, with a microstructure of interlocking β-Si_3N_4 crystal columnar, were fabricated by protein foaming method combined with sintered reaction-bonded method. For comparison, the ordinary protein foamed ceramics with irregular block microstructure were fabricated by reaction-bonded method, whose main phase was α-Si_3N_4. The thermal conductivity, compressive strength and high-temperature oxidation resistance of both types of samples were compared, and the following results were obtained: (1) The compressive strengths of both types of sintered samples were 3.6–20.5 MPa (ordinary samples fabricated by reaction-bonded method) and 13.2–45.9 MPa (self-reinforced samples fabricated by

sintered reaction-bonded method), respectively. When open porosity was about 80%, both types of Si_3N_4 ceramic foams had excellent thermal insulation properties (<0.15 W m^{-1} K^{-1}), but the compressive strength of in-situ self-reinforced samples increased by more than 158% compared with ordinary samples fabricated by reaction-bonded method. (2) Microstructures of both types of samples were deformed with increase in oxidation temperature. Furthermore, after oxidation temperature was increased to 1400 °C, oxidation weight gain decreased from 18.07% for ordinary samples to only 2.18% for self-reinforced samples, which greatly improved the high-temperature oxidation resistance of Si_3N_4 ceramic foams.

Declaration of competing interest

The authors declare that they have no known competing financial interests or personal relationships that could have appeared to influence the work reported in this paper.

Acknowledgements

This work was supported by the National Natural Science Foundation of China (No. 51802347), Natural Science Foundation of Hubei Province, China (No. 2018CFB183).

References

[1] B.I. Karawdeniya, Y.M.N.D.Y. Bandara, J.W. Nichols, R.B. Chevalier, J.R. Dwyer, Surveying silicon nitride nanopores for glycomics and heparin quality assurance, Nat. Commun. 9 (2018) 3278, https://doi.org/10.1038/s41467-018-05751-y.

[2] A. Parsi, F. Golestani-Fard, S.M. Mirkazemi, The effect of gelcasting parameters on microstructural optimization of porous Si_3N_4 ceramics, Ceram. Int. 45 (2019) 9719–9725, https://doi.org/10.1016/j.ceramint.2019.01.222.

[3] A. Koen, J.P. George, V. Jochem, N. Kristiaan, K. Bart, V.T. Dries, B. Jeroen, Nanophotonic Pockels modulators on a silicon nitride platform, Nat. Commun. 9 (2018) 3444, https://doi.org/10.1038/s41467-018-05846-6.

[4] L. Yin, X. Zhou, J. Yu, H. Wang, Preparation of silicon nitride foam with three-dimensional interconnected pore structure, Mater. Des. 89 (2016) 620–625, https://doi.org/10.1016/j.matdes.2015.10.020.

[5] I. Khader, C. Koplin, C. Schröder, J. Stockmann, A. Kailer, Characterization of a silicon nitride ceramic material for ceramic springs, J. Eur. Ceram. Soc. 40 (2020) 3541–3554, https://doi.org/10.1016/j.jeurceramsoc.2020.03.046.

[6] K. Mcgarrity, P. Tumurugoti, K. Ning, H. Shulman, Fractography of silicon nitride based ceramics to guide process improvements, J. Eur. Ceram. Soc. 40 (2020) 4746–4752, https://doi.org/10.1016/j.jeurceramsoc.2020.02.017.

[7] K. Balázsi, M. Furkó, Z. Liao, J. Gluch, C. Balázsi, Porous sandwich ceramic of layered silicon nitride-zirconia composite with various multilayered graphene content, J. Alloys Compd. 832 (2020) 154984, https://doi.org/10.1016/j.jallcom.2020.154984.

[8] L. Yin, X. Zhou, J. Yu, H. Wang, Effect of rotating speed during foaming procedure on the pore size distribution and property of silicon nitride foam prepared by using protein foaming method, Ceram. Int. 43 (2017) 4096–4101, https://doi.org/10.1016/j.ceramint.2016.12.003.

[9] D. Das, K. Nijhuma, A.M. Gabriel, G.P.F. Daniel, D.D.M.I. Murilo, Recycling of coal fly ash for fabrication of elongated mullite rod bonded porous SiC ceramic membrane and its application in filtration, J. Eur. Ceram. Soc. 40 (2020) 2163–2172, https://doi.org/10.1016/j.jeurceramsoc.2020.01.034.

[10] N.M. Raheleh, M.D. Pugh, D.A.L. Robin, Formation mechanism of porous reaction-bonded silicon nitride with interconnected pores in the presence of MgO, J. Eur. Ceram. Soc. 39 (2019) 915–927, https://doi.org/10.1016/j.jeurceramsoc.2018.10.032.

[11] S. Morita, M. Iijima, J. Tatami, Microstructural control of green bodies prepared from Si-based multi-component non-aqueous slurries and their effects on fabrication of Si3N4 ceramics through post-reaction sintering, Adv. Powder Technol. 29 (2018) 3199–3209, https://doi.org/10.1016/j.apt.2018.08.026.

[12] S.S. Mishra, D. Chaira, S.K. Karak, Effect of Y_2O_3 and Al_2O_3 sintering additives during fabrication of Si_3N_4-Mo-Si cermet by conventional pressure-less sintering, Ceram. Int. 45 (2019) 20555–20565, https://doi.org/10.1016/j.ceramint.2019.07.035.

[13] N. Soltani, S. Soltani, A. Bahrami, M.I. Pech-Canul, A. Gurlo, Electrical and thermomechanical properties of CVI-Si_3N_4 porous rice husk ash infiltrated by Al-Mg-Si alloys, J. Alloys Compd. 696 (2017) 856–868, https://doi.org/10.1016/j.jallcom.2016.12.051.

[14] A. Kumar, A. Gokhale, S. Ghosh, S. Aravindan, Effect of nano-sized sintering additives on microstructure and mechanical properties of Si_3N_4 ceramics, Mat. Sci. Eng. A 750 (2019) 132–140, https://doi.org/10.1016/j.msea.2019.02.020.

[15] T. Liu, C. Jiang, W. Guo, Effect of CeO_2 on low temperature pressureless sintering of porous Si_3N_4 ceramics, J. Rare Earths 35 (2017) 172–176, https://doi.org/10.1016/S1002-0721(17)60896-2.

[16] C. Chen, X. Liang, M. Luo, S. Zhou, J. Ji, Z. Huang, M. Xu, Preparation and characterization of porous Si_3N_4-bonded SiC ceramics and morphology change mechanism of Si_3N_4 whiskers, Ceram. Int. 45 (2019) 5922–5926, https://doi.org/10.1016/j.ceramint.2018.12.060.

[17] E. Drouelle, V. Brunet, J. Cormier, P. Villechaise, S. Dubois, Microstructure-oxidation resistance relationship in Ti_3AlC_2 MAX phase, J. Alloys Compd. 826 (2020) 154062, https://doi.org/10.1016/j.jallcom.2020.154062.

[18] L. Sun, C. Liu, J. Zhang, J. Fang, Joining pre-oxidized dense Si_3N_4 to porous Si_3N_4 with β-spodumene based glass-ceramic interlayer, Appl. Surf. Sci. 481 (2019) 515–523, https://doi.org/10.1016/j.apsusc.2019.03.124.

[19] A. Qadir, Z. Fogarassy, Z.E. Horváth, K. Balazsi, C. Balazsi, Effect of the oxidization of Si_3N_4 powder on the microstructural and mechanical properties of hot isostatic pressed silicon nitride, Ceram. Int. 44 (2018) 14601–14609, https://doi.org/10.1016/j.ceramint.2018.05.081.

[20] W. Duan, D. Jia, D. Cai, B. Niu, Y. Zhou, A facile strategy for fabricating self-sealing dense coating grown in-situ on porous silicon nitride ceramics, J. Eur. Ceram. Soc. 41 (2020) 2162–2167, https://doi.org/10.1016/j.jeurceramsoc.2020.10.040.

[21] L.M. Lenz, G. Barroso, M. Parchovianský, D. Galusek, E. Ionescu, W. Krenkel, G. Motz, Synthesis and characterization of yttrium and ytterbium silicates from their oxides and an oligosilazane by the PDC route for coating applications to protect Si_3N_4 in hot gas environments, J. Eur. Ceram. Soc. 37 (2017) 5177–5191, https://doi.org/10.1016/j.jeurceramsoc.2017.04.034.

[22] L. Wang, G. He, Z. Yang, H. Zhao, J. Zhao, J. Li, Combustion synthesis of α-Si_3N_4 powders using in-situ nano-SiO_2 coated Si and Si_3N_4 reactants, Ceram. Int. 47 (2021) 4854–4857, https://doi.org/10.1016/j.ceramint.2020.10.057.

[23] S. Farhan, R. Wang, K. Li, Physical, thermal and ablative performance of CVI densified urethane-mimetic SiC preforms containing in situ grown Si_3N_4 whiskers, J. Eur. Ceram. Soc. 37 (2017) 499–508, https://doi.org/10.1016/j.jeurceramsoc.2016.09.008.

[24] Z. Chai, J. Ding, C. Deng, H. Zhu, G. Li, C. Yu, Ni-catalyzed synthesis of hexagonal plate-like alpha silicon nitride from nitridation of Si powder in molten salt media, Adv. Powder Technol. 27 (2016) 1637–1644, https://doi.org/10.1016/j.apt.2016.05.027.

[25] Y. Zhang, D. Yao, K. Zuo, Y. Xia, J. Yin, H. Liang, Y. Zeng, Effects of N_2 pressure and Si particle size on mechanical properties of porous Si_3N_4 ceramics prepared via SHS, J. Eur. Ceram. Soc. 40 (2020) 4454–4461, https://doi.org/10.1016/j.jeurceramsoc.2020.05.038.

[26] V.K. Sarin, On the α-to-β phase transformation in silicon nitride, Mat. Sci. Eng. A 105–106 (1988) 151–159, https://doi.org/10.1016/0025-5416(88)90491-0.

[27] B. Wang, Q. Jiang, W. Liu, Z. Zhu, S. Wu, Fabrication of fine-grained α/β Si_3N_4 by hot pressing flowing sintering at 1550 °C, Ceram. Int. 45 (2019) 13958–13963, https://doi.org/10.1016/j.ceramint.2019.04.094.